Macromolecules

pubs.acs.org/Macromolecules Article

# Interparticle Interactions of Dendrimer, Comb, and Linear Grafted Nanoparticles via Coarse-Grained Molecular Dynamics Simulations

Pouria Nourian, Jimmy Lawrence, and Andrew J. Peters*

Cite This: https://doi.org/10.1021/acs.macromol.4c00235 Read Online

ACCESS | Metrics & More | Article Recommendations | Supporting Information

**ABSTRACT:** Rational approaches to impart a robust organic interface on nanoparticle (NP) surfaces for increasing the NP stability and repulsion are critical for advancing nanocomposite-based technologies. However, for applications where the choice of NP cores, binding groups, and ligand chemistry is restricted, the molecular parameter of polymer ligands becomes a crucial design variable. Here, we employ coarse-grained molecular dynamics simulations to examine the effect of ligand architecture, grafting density, and NP size on the dispersion behavior of polymer-grafted NPs. Among the ligand architectures studied (linear, dendron, and comb), comb ligands with short backbones (BBs) and high side chain densities (SCDs) (i.e., number of side chains per BB bead) yield the highest magnitude of repulsion at small interparticle distances followed by the dendrimer ligands and comb ligands with low SCD. Overall, our results underline the importance of precision design for brush ligands to dramatically improve the dispersion behavior and long-term stability of polymer-covered 'hairy' NPs.

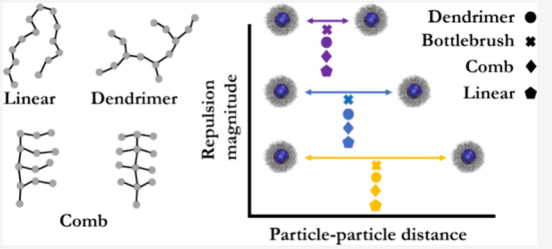




## 1. INTRODUCTION

Embedding small (micron or nanosized) fillers in the polymer matrix enhances the intrinsically lower mechanical properties of polymers without compromising the desired benefits of polymers such as ductility and low weight.[1,2] For example, PEEK reinforced with zirconia has been demonstrated to almost double the storage modulus of the composite at low temperatures,[3] while PEEK reinforced with PEI-modified boron nitride nanoparticles (NPs) showed significant increases in tensile strength elongation at break and thermal conductivity.[4] In addition to enhanced mechanical properties, polymer-nanoparticle composites (PNCs) display improved thermomechanical stability, charge transport, and cyto-/biocompatibility due to synergistic interactions between the inorganic NP core and the organic polymer interface.[5,6] Thus, the use of PNCs as advanced alternatives to pure polymers has increased in emerging technological applications such as flexible electronics,[7,8] heterogeneous catalysis,[9−11] bio/chemical sensing,[12−14] food packaging, biomedical devices,[15−21] and drug/molecule delivery.[22−26] Consequently, the performance of PNCs strongly depends on the dispersibility and stabilization of the NPs.

The enhanced properties of PNCs compared to that of their constituents are attributed to the strong interfacial interactions between the polymer matrix and NP fillers, as seen in the formation of interphase layers around the NPs.[27−30] Well-defined interphase layers are only achieved when the composite possesses a large interfacial surface area per unit volume, i.e., when NP fillers are uniformly dispersed inside the host polymer matrix.[31,32] The disruption of this layer leads to the deterioration of PNC performance and is primarily attributed to irreversible NP aggregation.[33,34] Grafting ligands on NP surfaces allows for controlling the spatial distribution of NPs to achieve desirable properties in PNCs. Such control over the dispersion behavior can be achieved via various parameters such as ligand and matrix polymer chemistry and molecular parameters, grafting density, NP size, and even polymer functionalization as shown by computational and experimental studies.[35−54] However, for various applications such as dispersants, flexible electronics, and sensing, the choice of NP cores, binding groups, and ligand chemistry are already limited, leaving the molecular parameter of polymer ligands as a design variable that can be broadly tailored to increase NP stability and repulsion.[55−59]

The molecular parameters of polymer ligands, including their binding strength, determine the magnitude of their steric repulsion and ligand density (number of ligands per nm$^2$). The binding nature of surface ligands can be covalent (e.g., silane groups on $SiO_2$ NPs[60]), or a robust but noncovalent one (e.g., thiol/carboxylate/amine groups on Au NPs[56,58]). The latter is notable for allowing one type of surface ligand to be exchanged with another while preventing NP aggregation. The combination of the 3D volume occupied by the polymer ligands and their surface mobility enables the organic layer to rearrange

Received: January 29, 2024
Revised: April 29, 2024
Accepted: May 9, 2024

under different conditions, making polymer grafting one of the most versatile and scalable strategies to improve the solution stability of NPs. Polymer-covered NPs are traditionally prepared through metal precursor reduction in the presence of polymer ligands or ligand exchange to afford densely grafted 'hairy' nanoparticles (HNP). HNPs are increasingly used as dispersible fillers in emerging technological applications such as filtration membranes,[61,62] structural applications,[63] and mixed matrix membranes.[64]

Simulation and experiment support improving steric stabilization through increased polymer grafting density,[46,65,66] with the upper limit of grafting density for polymer ligands being ~0.7 chains/nm$^2$ (determined from thermogravimetric analysis of NPs rigorously purified from excess ligands).[67] However, recent developments in the synthesis of branched and topological polymer architectures have opened up new strategies to impart robust polymeric layer coverage to NP surfaces through a minimal number of grafted ligands. Among these new architectures are dendrons and comb-type surface ligands. Dendrimers or dendrons are highly branched polymers with fractal-like shapes and exponentially increasing molecular weights per generation.[68] Comb polymers are made up of a linear backbone (BB) densely grafted with polymeric side chains (SCs). Modular synthetic strategies have enabled each structural parameter of dendritic and comb polymers (branching number, BB length, SC length), thus their functions and properties, to be tuned with high precision through judicious choice of molecular building blocks and macromonomers.[69] Further advances, as we recently reported, have enabled topologically uniform and discrete comb polymers to be synthesized, allowing even greater control over material properties and responses through designer structures.[70] Recent studies focused on the properties of these polymer classes[71−74] have indicated that although these classes are distinctly different, both have potential use in the creation of HNPs with high grafting density and potentially better dispersion characteristics. Modica et al.[69] studied the effect of comb polymers on interparticle attraction in the athermal limit and found an increased attraction caused by greater crowding of the polymer and subsequent poor wetting of the grafted layer. LaNasa and Hickey have demonstrated the ability to synthesize comb grafts using ring-opening metathesis polymerization and suggest a variety of other grafts are possible in a similar manner.[75] However, a clear picture of how the structural parameters of dendrimers and combs are correlated to the dispersion characteristics does not exist. With experimental samples having their structural accuracy improved over time, here we sought to examine the performance of precision branched polymers; by comparing the ability of linear and branched polymer ligands in improving the dispersibility of NPs, the results of which will provide valuable insights for future experimental studies.

In particular, we focus on three ligand architectures: linear, dendrimer, and comb (Figure 1a) and analyze the contribution of various parameters including BB and SC length, side chain density (SCD), and grafting density. Here, we clarify that throughout this paper, grafting density refers to the number of ligands attached to the surface of a NP, while SCD refers to the number of SCs attached to each individual BB bead of an individual ligand. We create systems with two polymer-grafted NPs in an explicitly defined solvated environment, while designing the ligand−NP interactions such that the ligands can freely migrate over the surface of the nanoparticle (Figure 1b),

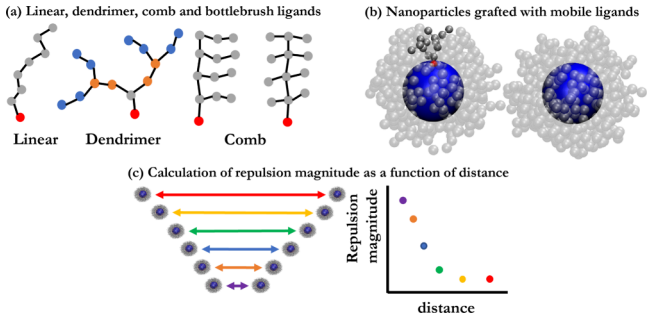


**Figure 1.** (a) Schematics of linear, dendrimer, and comb ligands with low and medium SCD. The anchoring graft beads are colored red. Dendrons of different generations have different colors. (b) Schematics of dendrimer ligands grafted on NPs. (c) Schematic of PMF calculations.

to reflect the well-documented surface mobility of thiol-based ligands on a gold surface.[76−80] Additionally, a system composed of two bare particles (i.e., no ligands) was simulated as a control case. We employ coarse-grained MD simulations to calculate the potential of mean force (PMF) and quantify the interactions between the two polymer-grafted NPs (Figure 1c). The PMF is a useful tool for quantifying the effective interactions between the NPs and has previously been used to study the effect of polydispersity of grafted chains,[81] the molecular weight of polymer matrix,[82] and chain length of polymer matrix[40] on the effective interactions between polymer-grafted NPs in polymer matrices.

## 2. METHODOLOGY

**2.1. Ligand Structures.** Different variations of three ligand architectures (linear, dendrimer, and comb) were deliberately designed to have a similar total number of monomers, except for a short linear ligand simulated at higher grafting density. Two different groups of linear chains, one that is made up of 7 beads (L-7) and one that is made up of 14 beads (L-14), are used (Figure 1a). Dendritic ligands are made up of third-generation dendrons that are composed of dimeric segments, thus resulting in each chain having a total of 14 beads (designated D3). As for the comb ligands, 11 different structures with a different number of BB beads (i.e., BB length), SC beads (i.e., SC length), and SCD are studied in this work. Ligands with a SCD of 1 are designated as low SCD, those with a SCD of 2 are designated as medium SCD, and any ligands with a SCD of 3 or greater are designated as high SCD. The comb ligands are labeled based on their BB and SC lengths as well as their SCD. For example, a comb ligand with 3 BB beads, 3 SC beads, and a SCD of 1 is labeled C-3-3-1. These ligands are composed of 13−16 beads per chain (Table 1 and Figure 2).

**2.2. Simulation Details.** The model used consists of three different particle types: one representing polymer beads, one representing the solvent, and one representing the NPs. The polymer was modeled using beads of diameter $\sigma$. Here, $\sigma$ represents the size of a polymer bead. For example, the L-14 ligand corresponds to a polystyrene chain with an averaged number molecular weight of 10 kDa. For this model, $\sigma \sim 1.5$ nm[83] (see SI for detailed description). Polymer beads are bonded together using finitely extensible nonlinear elastic (FENE) bonds[84]:


https://doi.org/10.1021/acs.macromol.4c00235
Macromolecules XXXX, XXX, XXX−XXX

**Table 1. Molecular Parameters of Ligands Used in this Study**[a]

| type | name | repeat units ($N$) | | | $N_{total}$ |
|---|---|---|---|---|---|
| linear | L-7 | 7 | | | 8 |
| | L-14 | 14 | | | 15 |
| type | name | $N_{beads/gen}$ | generation | | $N_{total}$ |
| dendritic | D3 | 2 | 3 | | 14 |
| type | name | $N_{backbone}$ | $N_{side\ chain}$ | $z$ | $N_{total}$ |
| Comb−low $z$ (SCD ($z$) = 1) | C-3-3-1 | 3 | 3 | 1 | 13 |
| | C-4-2-1 | 4 | 2 | 1 | 13 |
| | C-6-1-1 | 6 | 1 | 1 | 13 |
| | C-7-1-1 | 7 | 1 | 1 | 15 |
| Comb−medium $z$ (SCD ($z$) = 2) | C-2-3-2 | 2 | 3 | 2 | 15 |
| | C-3-2-2 | 3 | 2 | 2 | 16 |
| | C-4-1-2 | 4 | 1 | 2 | 13 |
| Comb−high $z$ (SCD ($z$) > 3) | C-2-2-3 | 2 | 2 | 3 | 15 |
| | C-2-1-6 | 2 | 1 | 6 | 15 |
| | C-3-1-3 | 3 | 1 | 3 | 13 |
| | C-3-1-4 | 3 | 1 | 4 | 16 |

[a] $N_{total}$: the total number of beads per chain. $N_{beads/gen}$: the number of beads per generation of the dendritic ligand. $N_{backbone}$, $N_{side\ chain}$, and $z$ are the BB length, SCD, and the SCD of the comb ligands, respectively. All comb ligands were denoted as C-$x$-$y$-$z$. The subscripts $x$, $y$, and $z$ represent $N_{backbone}$, $N_{side\ chain}$, and $z$.

$$U_{FENE}(r) = -\frac{1}{2}kr_0^2 \ln\left[1 - \left(\frac{r-\Delta}{r_0}\right)^2\right] \quad (1)$$

Here, a force constant of $k = 30$ and an equilibrium distance of $r_0 = 1.5$ is used. The nonbonded polymer beads as well as the solvent interact via the Lennard-Jones potential:

$$U_{LJ}(r) = 4\varepsilon\left[\left(\frac{\sigma}{r}\right)^{12} - \left(\frac{\sigma}{r}\right)^{6}\right] \quad (2)$$

where $r$ is the vector between particles, and $\varepsilon = k_BT$ with Boltzmann constant $k_B$ and temperature $T$. The $\varepsilon$ used for the solvent-solvent interaction was the same as that used for the solvent−polymer interaction. Moreover, a cutoff radius of $3\sigma$ was used for both interactions. Following reference,[83] this can correspond to a polystyrene chain with a bead size of 1.5 nm and a Kuhn segment length of 1.8 nm. The NPs were modeled in the fashion of Li et al.[85] NPs are considered spherical clusters of LJ beads of unit reduced density, $\rho^* = \rho_{NP}\sigma^3$, where $\rho_{NP}$ is the number density of LJ beads within each NP and set to $\sigma^{-3}$. Following Everaers and Ejtehadi,[86] the potential between NPs is found by integrating over all LJ particles in the two NPs and is

$$U_{NP,NP}(r) = U_A(r) + U_R(r) \quad (3)$$

where the attractive component, $U_A$, is

$$U_A(r) = -\frac{H_{NP-NP}}{6}\left[\frac{\sigma_{NP}^2}{2(r^2-\sigma_{NP}^2)} + \frac{\sigma_{NP}^2}{2r^2} + \ln\left(\frac{r^2-\sigma_{NP}^2}{r^2}\right)\right] \quad (4)$$

and the repulsive component, $U_R$, is

$$U_R(r) = \frac{H_{NP-NP}}{37{,}800}\frac{\sigma^6}{r}\left[\frac{r^2 - 7r\sigma_{NP} + 27\sigma_{NP}^2/2}{(r-\sigma_{NP})^7} + \frac{r^2 + 7r\sigma_{NP} + 27\sigma_{NP}^2/2}{(r+\sigma_{NP})^7} - \frac{2(r^2 - 15\sigma_{NP}^2/2)}{r^7}\right] \quad (5)$$

$H_{NP-NP}$ is the Hamaker constant and is evaluated as $4\pi^2\varepsilon_{NP}$. Experimental measurements[85−87] of the Hamaker constant for gold is ∼5 times that of polystyrene, so, following Li et al.,[85] $\varepsilon_{NP}$ is set to $5k_BT$ and therefore $H_{NP-NP} = 20\pi^2k_BT$. The potential between the NP and a polymer or solvent bead is found to be[86]:

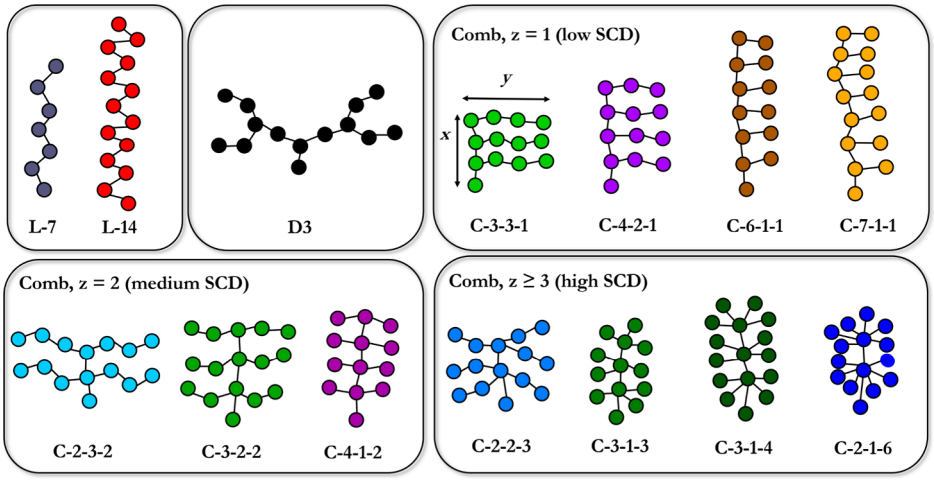


**Figure 2.** Ligand architectures simulated in this study (linear (L), dendritic (D), and comb polymers, denoted as C-$x$-$y$-$z$, where $x$: BB length, $y$: SC length, $z$: SCD). Different colors correspond to different BB lengths, while variations of the same color correspond to variations in SCDs.



https://doi.org/10.1021/acs.macromol.4c00235
Macromolecules XXXX, XXX, XXX−XXX

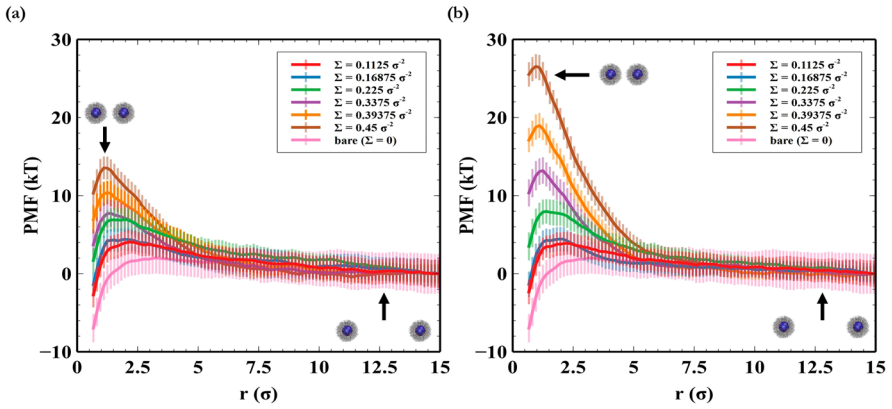


**Figure 3.** Plot of PMF versus the particle−particle distance ($r$) for (a) L-14 and (b) D3 systems at grafting densities ($\Sigma$) of $0.1125\sigma^{-2}$ (red), $0.16875\sigma^{-2}$ (blue), $0.225\sigma^{-2}$ (green), $0.3375\sigma^{-2}$ (purple), $0.39375\sigma^{-2}$ (orange), $0.45\sigma^{-2}$ (brown), and 0 (bare nanoparticle, pink). Vertical transparent lines represent statistical uncertainties.

$$U_{NP,P/S}(r) = \frac{\sigma_{NP}^3 \sigma^3 H_{NP-P/S}}{36\left(\frac{\sigma_{NP}^2}{4} - r^2\right)^3} \left[1 - \frac{(5\sigma_{NP}^6/64 + 45\sigma_{NP}^4 r^2/16 + 63\sigma_{NP}^2 r^4/4 + 15r^6)\sigma^6}{15(\sigma_{NP}/2 - r)^6(\sigma_{NP}/2 + r)^6}\right] \quad (6)$$

where $H_{NP-P/S} = 24\pi k_B T$.

In addition to studying the effect of polymer architecture, we also studied the effects of variation in particle size and grafting density are also studied. Five grafting densities of 0.1125, 0.16875, 0.225, 0.3375, 0.39875, and $0.45\sigma^{-2}$ (units of ligands per unit area, where the diameter of a polymer bead is $\sigma$) are considered for all the systems studied (except the L-7 systems the grafting densities for L-7 systems are doubled to keep total polymer content comparable). For the L-14 and D3 systems, the different particle diameters used are 3.33, 5, 6.67, and $8.33\sigma$, while only a particle diameter of $3.33\sigma$ is used for the comb and L-7 systems.

All the simulations were conducted using the HOOMD-blue software package.[88] For the particle−particle, particle−polymer, and particle−solvent potentials, the pair table function was used with a width of 1000 (that is, 1000 points are calculated and used to interpolate the force and potential). A cutoff of $\sigma_{NP} + 3.5\sigma$ was used for the particle−particle interaction, and a cutoff of $\frac{\sigma_{NP}}{2} + 3\sigma$ was used for the particle−polymer and particle−solvent interaction. A summary of all of the interaction parameters and cutoff radii can be found in the SI (Table S1). The constant number of particles, volume, and temperature (NVT) ensemble at a temperature of $T = 1$ and with a time step ($\Delta t$) of $0.01\tau$ was used, where $\tau = \frac{\sqrt{\varepsilon/m}}{\sigma}$. The time constant for the NVT integrator was set to $0.1\tau$. The graft points (i.e., anchoring beads) for each of the ligands were kept at a fixed distance from the centers of the particles using a distance constraint between said particle and the graft particle of the ligand. This allows the graft to move freely over the surface of the particle. Two cell-type neighbor lists were used to improve calculation efficiency because of the large difference in diameter between the particles. One was used for the polymer−polymer interactions and the other for the particle−polymer and particle−particle interactions.

NPs were built according to the specific architecture and grafting density with the grafts uniformly distributed across the surface of the particle, using an algorithm that had been used previously.[89] Two copies of these particles are placed $30\sigma$ apart along the $x$-axis in a simulation volume that is $60\sigma \times 40\sigma \times 40\sigma$. A harmonic potential:

$$U_{PMF}(r) = \frac{k_{PMF}}{2}(r - r_{0,PMF})^2 \quad (7)$$

between the NPs was applied. Initially, $k_{PMF} = 5$ and $r_{0,\,PMF} = 15 + \sigma_{NP}$ and the simulation was warmed up for a duration of $1000\tau$ (i.e., 100,000 steps using a time step of $0.01\tau$). This initial distance ensures no interaction between the NPs or their grafts and is the reference point for the PMF. The spring constant $k_{PMF}$ was then increased to 50, and $r_{0,\,PMF}$was decreased in increments of 0.2 for 81 steps, creating 81 potential windows for the PMF calculation. Each window was sampled for 100,000 steps (i.e., a duration of $1000\tau$) with snapshots of NP positions taken every 100 steps (i.e., every $1\tau$), leading to 1000 samples for every window. The PMF was calculated (Figure 1c) using the weighted histogram analysis method (WHAM)[90−92] and the code developed by Grossfield and coworkers[92] with a tolerance of 0.000001. Figure S1 plots the relative probability of distances for each window in a representative simulation. Good overlap is found between each window. The compression of windows at low distances is caused by the significant increase in the force required to continue pushing particles together.

## 3. RESULTS AND DISCUSSION

**3.1. PMF.** The PMF versus the particle spacing $r$ (i.e., the distance separating the facing surfaces of the two NPs) for the bare particle, linear L-14, and D3 systems with a NP radius of $3.33\sigma$ are presented in Figure 3, while the results for the low-SCD comb, medium-/high-SCD combs, and L-7 systems are presented in Figures S4−S6, respectively. The grafting densities studied are 0.1125, 0.16875, 0.225, 0.3375, 0.39375, and $0.45\sigma^{-2}$, which, based on a conversion of $\sigma \sim 1.5$ nm, translates to 0.05, 0.075, 0.1, 0.15, 0.175, and 0.2 $nm^{-2}$, respectively.

As two particles approach each other, the PMF between them increases sharply at a particle spacing of $\sim 4.7\sigma$, reaches its maximum value at $\sim 2$ to $2.5\sigma$ and decreases sharply as $r$ approaches zero. This sharp decrease can be attributed to the strong interparticle interaction, as they lose their polymer ligand shell (that is otherwise shielded by the polymer shell).


https://doi.org/10.1021/acs.macromol.4c00235
Macromolecules XXXX, XXX, XXX−XXX

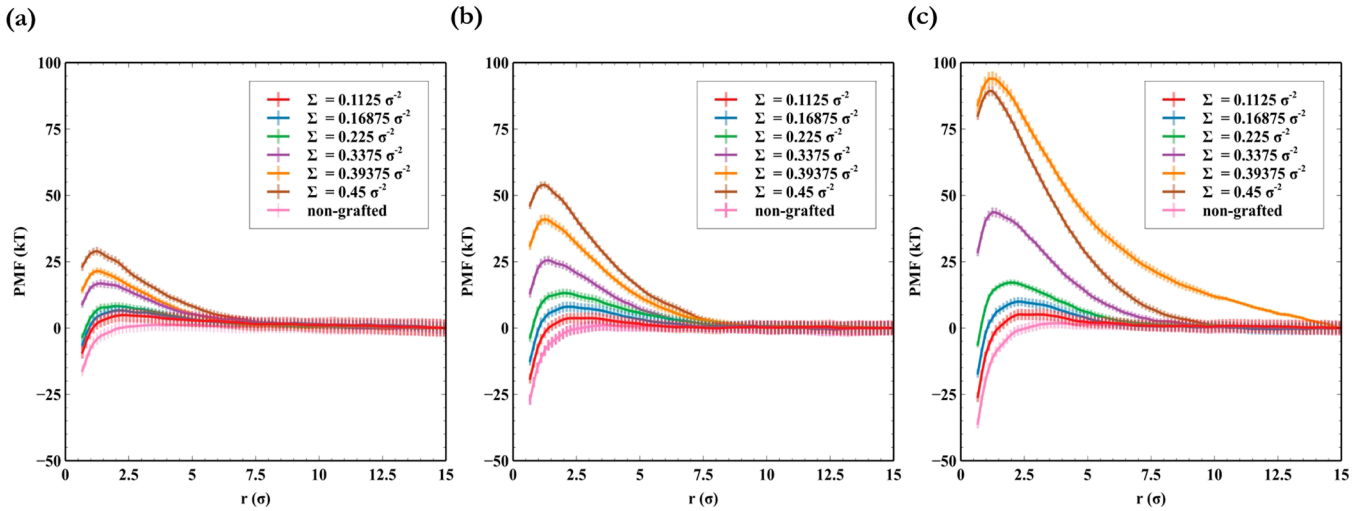


**Figure 4.** Plot of PMF vs the particle−particle distance ($r$) for L-14 systems with a NP diameter (a) $5\sigma$, (b) $6.67\sigma$, and (c) $8.33\sigma$ at grafting densities ($\Sigma$) of $0.1125\sigma^{-2}$ (red), $0.16875\sigma^{-2}$ (blue), $0.225\sigma^{-2}$ (green), $0.3375\sigma^{-2}$ (purple), $0.39375\sigma^{-2}$ (orange), $0.45\sigma^{-2}$ (brown), and 0 (bare NP, pink). Vertical transparent lines represent statistical uncertainties.

In particular, the onset of the increase in the PMF corresponds to the point where significant interactions between the grafted polymers on each particle become apparent. For comparison, the unperturbed end-to-end distance of the linear grafts ($\langle h \rangle_0 = \sqrt{n}\sigma$) is $3.6\sigma$. Therefore, significant ligand interaction should occur around approximately twice that distance at $7.2\sigma$. The PMF increases slightly smaller than this, partly due to the curvature of the particles, which increases the distance between most grafts. The peak occurs a little beyond a single polymer bead radius. Beyond this critical distance, because the polymer ligands are mobile on the NP surface, they will be effectively "pushed away", leaving no organic layer to shield the particle interactions, and the attractive force starts to dominate. This agrees with experimentally observed aggregation for NPs compressed under high pressure (>3 GPa).[93]

Notably, the increase in PMF (the energy cost to push the two particles toward each other) increases more rapidly for the dendrimer structure as compared to the linear structure for all of the grafting densities with decreasing $r$ (Figure 3). For example, the magnitude and onset of the interparticle repulsion increases with increasing ligand grafting density and is more significant in D3 systems when compared with L-14 systems at any given ligand grafting density. While this is expected, our result underscores the significance of ligand architecture for enhancing steric repulsion. Moreover, our calculation shows that there is a small repulsion effect even for particles with no ligands, presumably due to solvent−particle interactions. As the solvent beads are depleted from between the particles, there is a net potential energy loss until the particle−particle interaction dominates.

To examine the effect of NP size, we calculated the PMF for linear systems (L-14) for NPs having diameters of 5, 6.67, and $8.33\sigma$ (Figure 4). The results for the D3 systems with different particle diameters are presented in Figure S7. The PMF values are higher for larger particle diameters for a given grafting density. This is likely because the larger particles have a 'flatter' surface (because of a larger radius of curvature) and will have a higher total number of grafted chains for a given grafting density, resulting in a stronger repulsion).

Each of the PMFs in Figure 4 shows the same trend of sharply decreasing about $\sigma$ (i.e., 1 polymer bead diameter) separation between the particle surfaces. Interestingly, the onset of the PMF increase occurs at slightly larger distances, even after subtracting the particle diameters. While the PMF for the $3.33\sigma$ diameter particles began increasing at about $\sim 4.5\sigma$, the diameter $5\sigma$ particle PMF increases at $\sim 6\sigma$, while the $6.67\sigma$ diameter PMF increases at $\sim 7\sigma$ and the $8.33\sigma$ diameter PMF at $\sim 8\sigma$. This is caused by the decreased curvature of the particles, leading to more ligands interacting even when the particles are farther apart.

**3.2. Energy Barrier.** Having calculated the role of polymer architecture on PMF, next, we investigated the repulsion magnitude. Calculating the steric repulsion will give a quantitative idea of the steric barrier for NPs to aggregate. The magnitude of the close-range repulsion or the energy barrier ($\Delta F$) versus the grafting density for all the systems with a NP diameter of $3.33\sigma$ ($\approx$5 nm) is presented in Figure 5.

Generally, $\Delta F$ increases proportionally with the grafting density because the denser polymer interface imparts a higher energy penalty for flocculation and aggregation in the form of

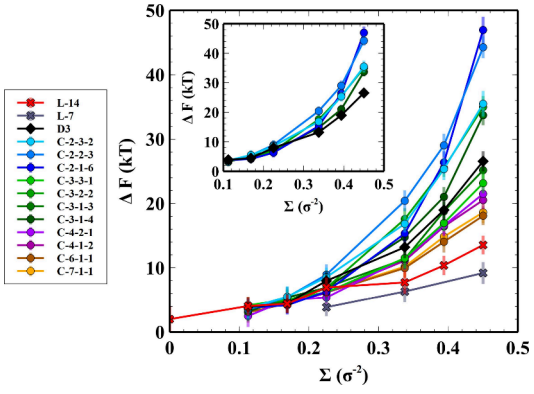


**Figure 5.** Plot of energy barrier ($\Delta F$) versus grafting density ($\Sigma$) for linear (crosses), dendrimer (diamonds), and comb (circles) systems. The coloring scheme is the same as the one described in Figure 2. Vertical transparent lines represent statistical uncertainties. Inset: Plot of $\Delta F$ versus $\Sigma$ for the dendrimer and five of the comb systems.


https://doi.org/10.1021/acs.macromol.4c00235
Macromolecules XXXX, XXX, XXX−XXX

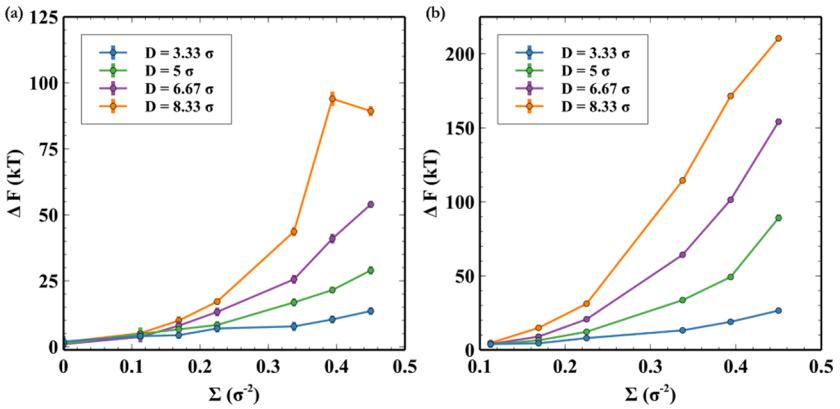


**Figure 6.** Plot of energy barrier ($\Delta F$) versus grafting density ($\Sigma$) for (a) L-14 and (b) D3 systems for NP of diameter of 3.33$\sigma$ (blue), 5$\sigma$ (green), 6.67$\sigma$ (purple), and 8.33$\sigma$ (orange). Vertical lines represent statistical uncertainties, which are mostly smaller than the data markers.

steric hindrance. Progressing from the highest overall steric hindrance, the comb polymer with two BB beads, two beads per SC, and three SCs per BB bead (C-2-2-3) has the highest $\Delta F$ at all but the highest grafting densities, followed by four other combs, the dendrimer, and the remaining systems. As expected, the linear ligand systems have the lowest steric repulsion, emphasizing the role of ligand architecture in influencing the repulsion between grafted NPs. Moreover, comb ligands with an architecture closest to that of linear ligands (C-6-1-1 and C-7-1-1) possess the lowest values of $\Delta F$ among the comb ligands. For comb polymers with the same BB length, increasing SCD (z) is more important than increasing SC length (y), as seen in C-2-2-3 vs C-2-3-2 (inset of Figure 5). Interestingly, the high z samples, such as C-2-2-6 and C-3-1-4, have a greater slope at high $\Sigma$, suggesting that high grafting densities of these architectures are especially effective at limiting particle interactions. In general, our results show that comb ligands with shorter BBs and higher z induce a repulsion that is stronger than that of the dendrimers (inset of Figure 5).

Next, we sought to determine the effect of NP size on steric repulsion. Values of $\Delta F$ for linear and dendrimer systems with various NP diameters are presented in Figure 6. As mentioned before, for all ligand grafting densities, $\Delta F$ increases with a larger NP diameter since the overall density of the interphase increases because of more chains being present on a bigger NP. Additionally, for smaller particles, the volume of shells a given distance away from the particle increases rapidly, while for larger particles this increase is reduced. This can be seen by calculating the surface area of a shell a distance $\Delta r$ away from the surface of a particle $\left(\mathrm{SA}_{\mathrm{Shell}} = \frac{4}{3}\pi\left(\frac{D}{2} + \Delta r\right)^3\right)$ relative to the surface area of the particle $\left(\mathrm{SA}_{\mathrm{Particle}} = \frac{4}{3}\pi\left(\frac{D}{2}\right)^3\right)$. After simplification, this ratio is $\mathrm{SA}_{\mathrm{Ratio}} = 1 + \left(\frac{\Delta r}{D/2}\right)^3$. As $D$ increases, the increase in surface area becomes smaller for a given $\Delta r$, so the chains remain more constrained and must pack densely at that distance.

Finally, we consider the effect of the total number of polymer beads since the nature of the comb and dendrimer topologies means that the total number of monomers per graft is not the same among dendrimers and combs studied here. The results for L-14, L-7, D3, and five comb ligands that have a higher $\Delta F$ than the D3 ligands (C-2-3-2, C-2-2-3, C-2-1-6, C-3-2-2, and C-3-1-4) are presented for comparison in Figure 7a. D3 and L-14 ligands are composed of 14 monomers, C-2-2-3,

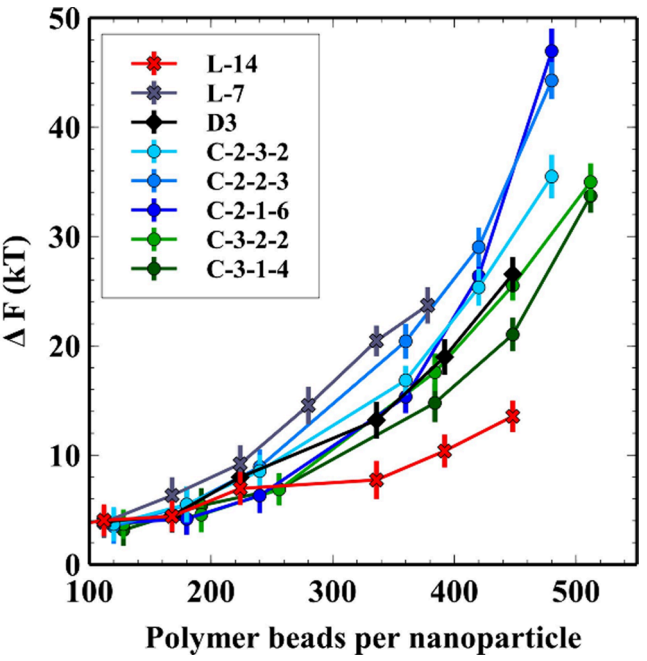


**Figure 7.** Plot of energy barrier ($\Delta F$) versus polymer beads per NP linear (cross), dendrimer (diamond), and five comb (circle) systems. Vertical lines represent statistical uncertainties.

C-2-3-2, and C-2-1-6 are composed of 15, and C-3-2-2 and C-3-1-4 are composed of 16 (Table 1). Interestingly, the shorter L-7 ligands result in the highest $\Delta F$ followed by the three comb systems with a BB length of 2 (i.e., C-2-$y$-$z$), then the dendritic D3 ligands followed by the comb systems with a BB length of 3 (i.e., C-3-$y$-$z$) and finally L14. The C-3-y-z systems are shifted right, resulting in lower $\Delta F$ values compared to those of other systems at the same total polymer content. The high repulsion in the L-7 system is likely due to a high density of polymers at the surface relative to other systems, consistent with existing literature.[36,66,94]

**3.3. Density of Polymer around the NP.** The above results suggest that the packing density of polymer monomers around the particle is the main driving force for steric repulsion. This also explains the minor energy barrier differences at low graft density because the architectural


https://doi.org/10.1021/acs.macromol.4c00235
Macromolecules XXXX, XXX, XXX−XXX

features that give rise to differences in polymer packing density are accentuated at high graft density but mitigated at low graft density. The L-7 system has the highest $\Delta F$ of all systems when comparing the total amount of polymer beads per particle because it restricts beads closer to the surface. A similar effect would explain why the dendrimer and comb systems with shorter BBs also have high $\Delta F$, since both these topologies reduce $R_g$ compared to linear polymers (see Figure S7). They might be expected to have higher density near the particle surface. To investigate this, we calculated the density of polymer beads as a function of distance from the surface for all of the systems with a NP diameter of $3.33\sigma$, when the two NPs are far apart. The results for the case with a grafting density of $0.45\sigma^{-2}$ are plotted in Figure 8, and the rest are shown in Figure S9. A bin size of $1\sigma$ is used for all of the calculations.

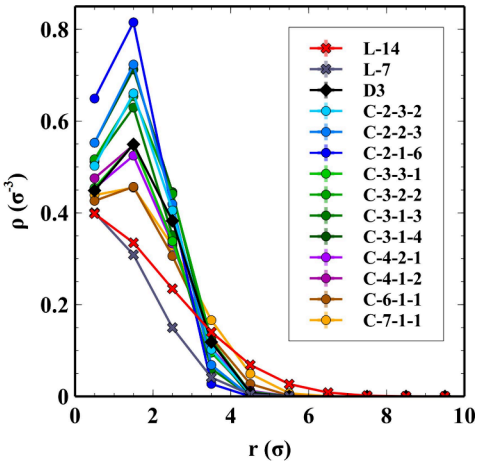


**Figure 8.** Plot of number density ($\rho$) versus distance from the particle surface ($r$) for the case with $D = 3.33\sigma$ and $\Sigma = 0.45\sigma^{-2}$ for linear (crosses), dendrimer (diamonds), and comb (circles) systems. The coloring scheme is the same as the one described in Figure 2. Vertical lines represent the standard errors, which are smaller than the data markers.

Due to the presence of SCs, all systems with branched ligands exhibit an increase in polymer density near the surface. For all the systems, polymer density diminishes as the distance from the surface increases, i.e., as the volume available for polymer beads to occupy increases. At a distance of $\sim 1.5\sigma$—the peak of the density histogram for all except the linear ligands—the densities correlate well with the $\Delta F$; combs have the highest values followed by dendrimers and linear ligands. The C-2-1-6 system exhibits the highest peak, corresponding to the largest $\Delta F$ at the grafting density of $0.45\sigma^{-2}$. Moreover, at a distance greater than $4\sigma$, the trend becomes reversed: L-14 has the highest densities followed by the comb ligands and the rest. The C-2-1-6 system has the highest peak in density histogram at all grafting densities, but its $\Delta F$ is not the highest at grafting densities besides $0.45\sigma^{-2}$. Overall, these trends indicate that comb (with medium to high SCD) and dendrimer systems have more beads packed close to the surface compared with comb (with low SCD) and linear systems. To investigate such observation further, the radius of gyration ($R_g$) was calculated for systems with a NP diameter of $3.33\sigma$ when the particles were far enough away as to be noninteracting, and the results are shown in Figure 9.

There is virtually no statistical difference with grafting density but significant differences between graft topologies. L-

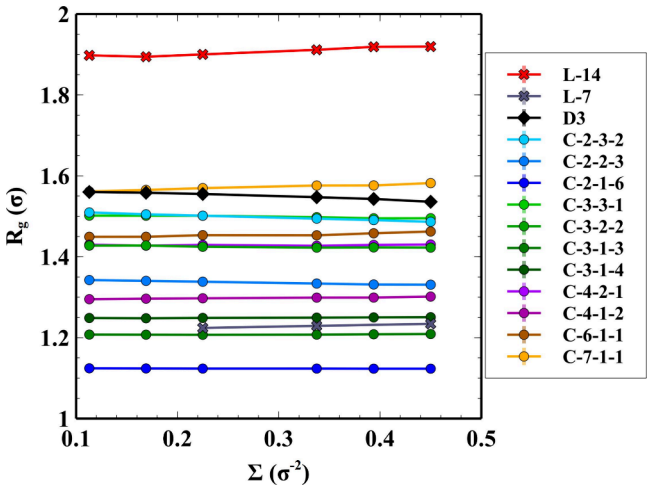


**Figure 9.** Plot of radius of gyration ($R_g$) versus grafting density ($\Sigma$) for linear (crosses), dendrimer (diamonds), and comb (circles) systems. The coloring scheme is the same as the one described in Figure 2. The vertical transparent lines represent the standard errors, which are mostly smaller in size than the data markers.

14, as expected, shows the highest $R_g$, while L-7, as expected, shows the lowest. The dendrimer and comb topologies show a significant decrease compared to the linear grafts, consistent with the increase in the density of polymer beads near the surface of the particle. The C-2-1-6 system has the lowest $R_g$ among all the ligands, which explains its corresponding high peak in the density histogram; short BB and SCs enable the ligands to be packed closer to the NP surface. It is evident that packing more polymer beads close to the surface leads to a larger $\Delta F$, and the architecture of ligands significantly affects such packing density. These trends are observed at all grafting densities and for systems with larger NPs. The statistical uncertainties become more significant as the grafting density decreases due to the smaller number of grafted chains per NP at lower grafting densities.

To investigate the invariance of $R_g$ with respect to the grafting density, we calculated a number of shape descriptors that are obtained from the gyration tensor.[95] A detailed description of these parameters and their values for all systems (Table S2) is presented in SI. We observed that *ligands with a higher degree of sphericity result in a stronger energy barrier* (Figure S13). A more spherically shaped graft will invariably exhibit a greater repulsion force than a more asymmetric graft, as they begin to overlap sooner. However, changes to the shape of the grafts with the graft density were minor. The minimum grafting density required to fully cover a NP of radius $R_{NP}$ with ligands having a radius of gyration of $R_g$,[96] which also has been described as the onset of stretching,[97] can be found as follows:

$$\Sigma_{min} = \frac{1}{\pi}\left(\frac{R_{NP} + R_g}{R_{NP}R_g}\right)^2 \quad (8)$$

For the L14 system, the ideal $R_g$ is about $1.53\sigma$ (considering each ligand as a freely joined chain, $R_g$ can be calculated as $N\sigma^2/6$). Thus, the $\Sigma_{min}$ for our L14 system with a NP diameter of $3.33\sigma$ is about $0.5\sigma^{-2}$, which is higher than the highest grafting density studied in this work. Thus, for the specific graft densities, particle sizes, and graft lengths used in this work, the perturbation of the graft shape is minimal. Larger particles or


https://doi.org/10.1021/acs.macromol.4c00235
Macromolecules XXXX, XXX, XXX−XXX

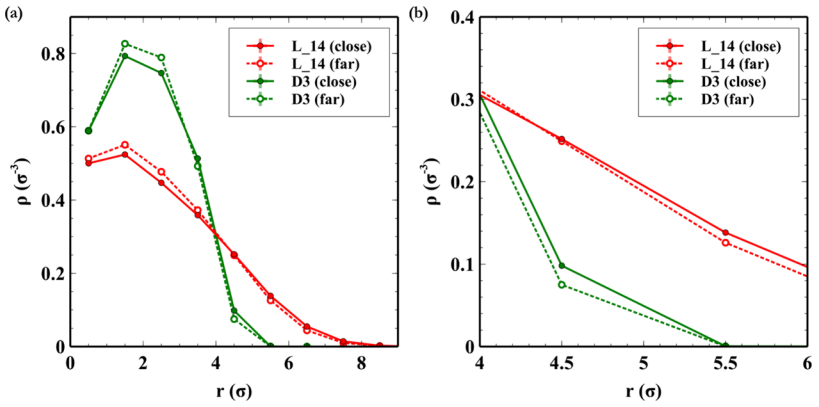


**Figure 10.** (a) Plot of number density ($\rho$) versus distance from the particle surface ($r$) for L-14 and D3 systems with $D = 8.33\sigma$ and $\Sigma = 0.45\sigma^{-2}$, and (b) zoom-in to $4 < r < 6$ from (a). Filled markers and solid lines represent data from when the two NPs are close, and hollow markers and dotted lines correspond to data from when they are far apart. Vertical lines represent the standard errors, which are smaller in size than the data markers.

longer grafts would perhaps exacerbate crowding and lead to a greater change in the graft shape.

The densities of polymer beads were also compared when the particles were far apart, and when they were close (close is defined as when $r_{0,\,PMF} \leq D + 1$) for the L-14 and D3 systems, a grafting density of $0.45\sigma^{-2}$ was also calculated and compared. A comparison for the case with a NP diameter of $8.33\sigma$ is shown in Figure 10, while the comparison for cases with other NP sizes is shown in Figure S10.

As the particles get close, polymer density far away from the particle increases (Figure 10b) likely because the grafts become more restricted because of the encroaching polymer and particle. Such a trend, while present at all grafting densities, is most noticeable at the highest grafting density and for the cases with the largest NP size. As mentioned earlier, statistical uncertainties associated with these calculations are more significant at lower grafting densities/for cases with smaller NPs due to a smaller number of total polymer beads being present in the system.

Moreover, given that the graft beads can move around on the surface of the NP, it is expected that the ability of the chains to move away from the NP surface would be affected by their ability to shift around the NP and vice versa. An example of this is shown in Figure 11 for the L-14 system at a grafting density of $0.45\sigma^{-2}$.

A clear bare spot is visible in Figure 11b where the grafts were pushed away from the particle−particle interface. Thus, the spatial configuration of the graft beads was also quantitively analyzed by assigning them to be either on the front or on the back of the NP, determining what fraction of those graft beads stayed in the front of the NPs or got pushed toward the back as the two NPs get close to each other.

The graft bead is designated as a front bead if the distance from the center-of-mass of the other NP to that bead is less than $\sqrt{d_{cc}^2 + D^2}$, where $d_{cc}$ is the distance between the two NPs' center of masses (i.e., it is located on the one-half of surface area of the NP that is closer to the other NP), and $D$ is the NP diameter. Given that the graft beads are initially uniformly distributed, the fraction of graft beads that are located on the front of a NP ($f_f$) is ∼ 0.5. We define a parameter $\Theta_f$ as the ratio of $f_f$ when the two NPs are close to $f_f$ at the beginning of the simulation (i.e., when the two NPs are far apart, and graft beads are distributed almost uniformly on the NP surface). As mentioned earlier, $f_f \sim 0.5$ is obtained when particles are far apart. Hence, $\Theta_f < 1$ indicates that the ligands have gotten pushed toward the back of the NPs when the two NPs are close. $\Theta_f$ versus the grafting density is plotted in Figure S11 for all the systems with a NP diameter of $3.33\sigma$. The results for the rest of the systems are presented in Figure S12. The comb ligands with medium and high SCD (especially C-2-2-3 and C-2-1-6 systems) show the highest resistance toward spatial reconfiguration of grafting beads (i.e., highest $\Theta_f$). In other words, more comb ligands tend to stay in front of NPs when the two NPs are close, thus resulting in a greater magnitude of polymer−polymer repulsion that contributes toward the NP dispersion. We must note that the noticeable statistical uncertainties associated with $\Theta_f$ are due to the relatively low number of chains grafted on each NP (which is at most 40 for systems with a NP diameter of $3.33\sigma$).

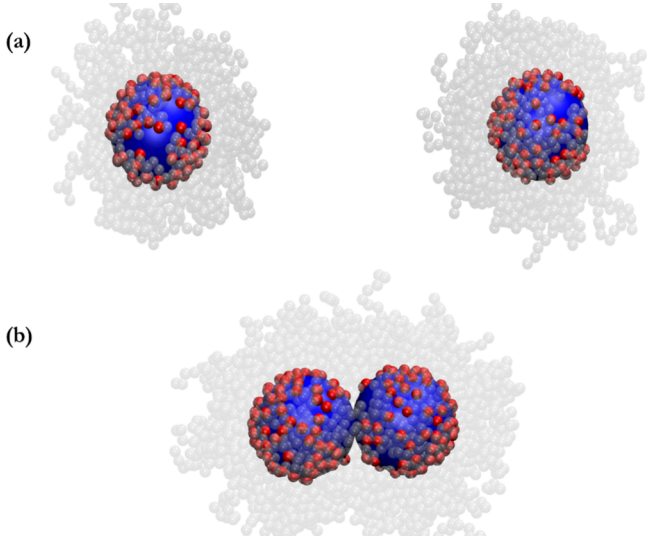


**Figure 11.** Illustration of (a) distribution of graft beads when the two NPs are far apart and (b) distribution of grafted ligands when the two NPs are close. The NPs, polymer beads, and grafted beads are colored blue, gray, and red, respectively. The polymer beads are depicted as transparent to improve visibility.

In summary, our observations indicate that the performance of grafted polymer chains in terms of their ability to induce a repulsion between the two NPs is governed (a) primarily by


https://doi.org/10.1021/acs.macromol.4c00235
Macromolecules XXXX, XXX, XXX−XXX

their packing density close to the surface of the NP and (b) secondarily by the conformational properties of the ligands, both of which are in turn influenced by the architecture of the ligands.

## 4. CONCLUSIONS

Using molecular dynamics simulations, the dispersion behavior of the polymer-grafted NPs as a function of polymer architecture, grafting density, and particle diameter was studied via analyzing the PMF at varying particle−particle distances.

Comb polymers with a short BB and high SCD yielded the largest repulsion force, whereas dendritic grafts exhibited a repulsion force comparable to that of medium BB length comb polymers and linear polymers showed the lowest repulsion. For experimentalists, the main point of this work may be that combs and dendrimers show a higher energy barrier to aggregation than linear polymers, suggesting that they will exhibit enhanced dispersion properties (when solvent−polymer interactions are the same as polymer−polymer interactions). Additionally, comb polymers can potentially surpass the efficacy of dendrimers with the benefit of a broader range of potential chemistries and fine-tuning of the chemistry and structure.

The repulsion strength was also observed to increase with an increasing grafting density and increasing particle diameter. Thus, increasing either the grafting density or the nanoparticle diameter will lead to an overall increase in the density of the grafted layer, which in turn results in an increase in the short-range repulsion between the two hairy nanoparticles.

The configurational changes in the polymer layer were also studied by calculating the density as a function of the distance from the particle around the nanoparticles. Moreover, the spatial configuration of graft beads was also analyzed by measuring the fraction of graft beads that are located on the front side of the nanoparticle when nanoparticles are close relative to those when they are far apart. The magnitude of particle−particle repulsion correlates decently with an increase in the polymer packing density close to the surface of the nanoparticle and a relatively lower decline in the fraction of graft beads located on the front of nanoparticles as particles, indicating that the particle−particle attraction overcomes the polymer−polymer repulsion through the ligands moving away from the surface and getting pushed toward the back of nanoparticles.

Overall, precision-synthesized comb polymers show performance surpassing that of dendrimers in terms of increasing the range and magnitude of induced repulsion between polymer-grafted nanoparticles. Comb polymers with various BB and SC lengths as well as different SCD were investigated in this work. It was found that decreasing the BB length while increasing the SCD generally increases the magnitude of the induced repulsion, while a higher SCD and short SCs may reduce the magnitude of induced repulsion at all but the highest grafting densities. Additionally, ligands with a higher degree of sphericity result in a stronger repulsion. The interplay among these parameters affecting the architecture of comb and bottlebrushes needs to be comprehensively studied to increase the potential of this type of polymer to be specifically engineered to have consistently better performance compared to other types of ligands, such as dendrimers, especially for application where design parameters such as ligand chemistry are limited.

## ASSOCIATED CONTENT

### Supporting Information

The Supporting Information is available free of charge at https://pubs.acs.org/doi/10.1021/acs.macromol.4c00235.

Representative WHAM calculations; calculation of correlation time used in the estimation of statistical uncertainties of PMF calculations; PMF for systems not included in the main text; density as a function of distance from the nanoparticle surface for systems that are not included in the main text; quantitative analysis of spatial conformation of graft beads ($\Theta_f$) for all systems; summary of model and interaction parameters; and analysis of shape descriptors derived from the gyration tensor (PDF)

## AUTHOR INFORMATION


### Corresponding Author

**Andrew J. Peters** − *Department of Chemical Engineering, Louisiana Tech University, Ruston, Louisiana 71270, United States;* orcid.org/0000-0001-5031-2828; Phone: (318) 257-5110; Email: apeters@latech.edu

### Authors

**Pouria Nourian** − *Department of Chemical Engineering, Louisiana Tech University, Ruston, Louisiana 71270, United States*

**Jimmy Lawrence** − *Department of Chemical Engineering, Louisiana State University, Baton Rouge, Louisiana 70803-2804, United States;* orcid.org/0000-0003-4455-6177

Complete contact information is available at: https://pubs.acs.org/10.1021/acs.macromol.4c00235


### Notes

The authors declare no competing financial interest.

## ACKNOWLEDGMENTS

This work was supported by the Louisiana Board of Regents under award LEQSF (2020-23)-RD-A-18. It was also partially supported by the US National Science Foundation under grant number OIA-1946231 the Louisiana Board of Regents for the Louisiana Materials Design Alliance (LAMDA). J.L. acknowledges the support from ACS Petroleum Research Fund (62656-DN17) and the National Institute of General Medical Sciences of the National Institutes of Health (R35GM151217). The high-performance computing resources were provided by the Louisiana Optical Network Initiative (https://loni.org).

## REFERENCES

(1) Winey, K. I.; Vaia, R. A. Polymer nanocomposites. *MRS bulletin* **2007**, *32* (4), 314−322.

(2) Jordan, J.; Jacob, K. I.; Tannenbaum, R.; Sharaf, M. A.; Jasiuk, I. Experimental trends in polymer nanocomposites—a review. *Materials Science and Engineering: A* **2005**, *393* (1), 1−11.

(3) Mishra, T.; Kumar, A.; Verma, V.; Pandey, K.; Kumar, V. PEEK composites reinforced with zirconia nanofiller. *Composites science and technology* **2012**, *72* (13), 1627−1631.

(4) Liu, X.; Gao, Y.; Shang, Y.; Zhu, X.; Jiang, Z.; Zhou, C.; Han, J.; Zhang, H. Non-covalent modification of boron nitride nanoparticle-reinforced PEEK composite: Thermally conductive, interfacial, and mechanical properties. *Polymer* **2020**, *203*, 122763.

(5) Kausar, A. A review of high performance polymer nanocomposites for packaging applications in electronics and food industries. *J. Plast. Film Sheet.* **2019**, *36* (1), 94−112.

(6) Lee, L. J.; Zeng, C.; Cao, X.; Han, X.; Shen, J.; Xu, G. Polymer nanocomposite foams. *Compos. Sci. Technol.* **2005**, *65* (15), 2344−2363.
(7) Lal, S.; Link, S.; Halas, N. J. Nano-optics from sensing to waveguiding. *Nature Photonics* **2007**, *1* (11), 641−648.
(8) Teranishi, T. Fabrication and electronic properties of gold nanoparticle superlattices. *Comptes Rendus Chimie* **2003**, *6* (8), 979−987.
(9) Remediakis, I. N.; Lopez, N.; Nørskov, J. K. CO Oxidation on Rutile-Supported Au Nanoparticles. *Angew. Chem. Int. Ed.* **2005**, *44* (12), 1824−1826.
(10) Remediakis, I. N.; Lopez, N.; Nørskov, J. K. CO oxidation on gold nanoparticles: Theoretical studies. *Appl. Catal. A: Gen.* **2005**, *291* (1), 13−20.
(11) Zhou, P.; Jia, S.; Pan, D.; Wang, L.; Gao, J.; Lu, J.; Shi, J.; Tang, Z.; Liu, H. Reversible Regulation of Catalytic Activity of Gold Nanoparticles with DNA Nanomachines. *Scientific Reports* **2015**, *5* (1), 14402.
(12) Alsawafta, M.; Badilescu, S.; Paneri, A.; Truong, V.-V.; Packirisamy, M. Gold-Poly(methyl methacrylate) Nanocomposite Films for Plasmonic Biosensing Applications. *Polymers* **2011**, *3* (4), 1833 DOI: 10.3390/polym3041833.
(13) Shinde, S.; Kim, D.-Y.; Saratale, R.; Syed, A.; Ameen, F.; Ghodake, G. A Spectral Probe for Detection of Aluminum (III) Ions Using Surface Functionalized Gold Nanoparticles. *Nanomaterials* **2017**, *7* (10), 287.
(14) Anker, J. N.; Hall, W. P.; Lyandres, O.; Shah, N. C.; Zhao, J.; Van Duyne, R. P. Biosensing with plasmonic nanosensors. *Nat. Mater.* **2008**, *7* (6), 442−453.
(15) Ribeiro, M.; Ferraz, M. P.; Monteiro, F. J.; Fernandes, M. H.; Beppu, M. M.; Mantione, D.; Sardon, H. Antibacterial silk fibroin/nanohydroxyapatite hydrogels with silver and gold nanoparticles for bone regeneration. *Nanomedicine: Nanotechnology, Biology and Medicine* **2017**, *13* (1), 231−239.
(16) Shevach, M.; Fleischer, S.; Shapira, A.; Dvir, T. Gold Nanoparticle-Decellularized Matrix Hybrids for Cardiac Tissue Engineering. *Nano Letters* **2014**, *14* (10), 5792−5796.
(17) Pérez-López, A. M.; Rubio-Ruiz, B.; Sebastián, V.; Hamilton, L.; Adam, C.; Bray, T. L.; Irusta, S.; Brennan, P. M.; Lloyd-Jones, G. C.; Sieger, D.; et al. Gold-Triggered Uncaging Chemistry in Living Systems. *Angewandte Chemie International Edition* **2017**, *56* (41), 12548−12552.
(18) Nascimento, H. P. O.; Oliveira, M. D. L.; de Melo, C. P.; Silva, G. J. L.; Cordeiro, M. T.; Andrade, C. A. S. An impedimetric biosensor for detection of dengue serotype at picomolar concentration based on gold nanoparticles-polyaniline hybrid composites. *Colloids and Surfaces B: Biointerfaces* **2011**, *86* (2), 414−419.
(19) Palza, H. Antimicrobial Polymers with Metal Nanoparticles. *Int. J. Mol. Sci.* **2015**, *16* (1), 2099.
(20) Firoz Babu, K.; Dhandapani, P.; Maruthamuthu, S.; Anbu Kulandainathan, M. One pot synthesis of polypyrrole silver nanocomposite on cotton fabrics for multifunctional property. *Carbohydr. Polym.* **2012**, *90* (4), 1557−1563.
(21) España-Sánchez, B. L.; Ávila-Orta, C. A.; Padilla-Vaca, F.; Neira-Velázquez, M. G.; González-Morones, P.; Rodríguez-González, J. A.; Hernández-Hernández, E.; Rangel-Serrano, Á.; Barriga-C, E. D.; Yate, L.; et al. Enhanced Antibacterial Activity of Melt Processed Poly(propylene) Ag and Cu Nanocomposites by Argon Plasma Treatment. *Plasma Process. Polym.* **2014**, *11* (4), 353−365.
(22) Li, Z.; Ye, E.; David; Lakshminarayanan, R.; Loh, X. J Recent Advances of Using Hybrid Nanocarriers in Remotely Controlled Therapeutic Delivery. *Small* **2016**, *12* (35), 4782−4806.
(23) Edwardson, T. G. W.; Lau, K. L.; Bousmail, D.; Serpell, C. J.; Sleiman, H. F. Transfer of molecular recognition information from DNA nanostructures to gold nanoparticles. *Nature Chemistry* **2016**, *8* (2), 162−170.
(24) Gupta, R.; Rai, B. Effect of Size and Surface Charge of Gold Nanoparticles on their Skin Permeability: A Molecular Dynamics Study. *Scientific Reports* **2017**, *7* (1), 45292.
(25) Ghosh, P.; Han, G.; De, M.; Kim, C. K.; Rotello, V. M. Gold nanoparticles in delivery applications. *Adv. Drug Delivery Rev.* **2008**, *60* (11), 1307−1315.
(26) Ding, Y.; Jiang, Z.; Saha, K.; Kim, C. S.; Kim, S. T.; Landis, R. F.; Rotello, V. M. Gold Nanoparticles for Nucleic Acid Delivery. *Molecular Therapy* **2014**, *22* (6), 1075−1083.
(27) Zare, Y.; Rhee, K. Y. A simple methodology to predict the tunneling conductivity of polymer/CNT nanocomposites by the roles of tunneling distance, interphase and CNT waviness. *RSC Advances* **2017**, *7* (55), 34912−34921.
(28) Rafiee, R.; Pourazizi, R. Influence of CNT functionalization on the interphase region between CNT and polymer. *Comput. Mater. Sci.* **2015**, *96*, 573−578.
(29) Zare, Y.; Rhee, K. Y. Development of a conventional model to predict the electrical conductivity of polymer/carbon nanotubes nanocomposites by interphase, waviness and contact effects. *Composites Part A: Applied Science and Manufacturing* **2017**, *100*, 305−312.
(30) Herasati, S.; Zhang, L. C.; Ruan, H. H. A new method for characterizing the interphase regions of carbon nanotube composites. *International Journal of Solids and Structures* **2014**, *51* (9), 1781−1791.
(31) Rong, M. Z.; Zhang, M. Q.; Ruan, W. H. Surface modification of nanoscale fillers for improving properties of polymer nanocomposites: a review. *Mater. Sci. Technol.* **2006**, *22* (7), 787−796.
(32) Fu, S.; Sun, Z.; Huang, P.; Li, Y.; Hu, N. Some basic aspects of polymer nanocomposites: A critical review. *Nano Materials Science* **2019**, *1* (1), 2−30.
(33) Jouault, N.; Vallat, P.; Dalmas, F.; Said, S.; Jestin, J.; Boué, F. Well-Dispersed Fractal Aggregates as Filler in Polymer−Silica Nanocomposites: Long-Range Effects in Rheology. *Macromolecules* **2009**, *42* (6), 2031−2040.
(34) Esbati, A. H.; Irani, S. Effect of functionalized process and CNTs aggregation on fracture mechanism and mechanical properties of polymer nanocomposite. *Mechanics of Materials* **2018**, *118*, 106−119.
(35) Jayaraman, A.; Schweizer, K. S. Effective Interactions and Self-Assembly of Hybrid Polymer Grafted Nanoparticles in a Homopolymer Matrix. *Macromolecules* **2009**, *42* (21), 8423−8434.
(36) Smith, G. D.; Bedrov, D. Dispersing Nanoparticles in a Polymer Matrix: Are Long, Dense Polymer Tethers Really Necessary? *Langmuir* **2009**, *25* (19), 11239−11243.
(37) Kalb, J.; Dukes, D.; Kumar, S. K.; Hoy, R. S.; Grest, G. S. End grafted polymer nanoparticles in a polymeric matrix: Effect of coverage and curvature. *Soft Matter* **2011**, *7* (4), 1418−1425.
(38) Shen, J.; Liu, J.; Gao, Y.; Cao, D.; Zhang, L. Revisiting the Dispersion Mechanism of Grafted Nanoparticles in Polymer Matrix: A Detailed Molecular Dynamics Simulation. *Langmuir* **2011**, *27* (24), 15213−15222.
(39) Nair, N.; Wentzel, N.; Jayaraman, A. Effect of bidispersity in grafted chain length on grafted chain conformations and potential of mean force between polymer grafted nanoparticles in a homopolymer matrix. *The Journal of Chemical Physics* **2011**, *134* (19), 194906.
(40) Meng, D.; Kumar, S. K.; Lane, D.; M, J; Grest, G. S Effective interactions between grafted nanoparticles in a polymer matrix. *Soft Matter* **2012**, *8* (18), 5002−5010.
(41) Jayaraman, A.; Schweizer, K. S. Effective Interactions, Structure, and Phase Behavior of Lightly Tethered Nanoparticles in Polymer Melts. *Macromolecules* **2008**, *41* (23), 9430−9438.
(42) Harton, S. E.; Kumar, S. K. Mean-field theoretical analysis of brush-coated nanoparticle dispersion in polymer matrices. *Journal of Polymer Science Part B: Polymer Physics* **2008**, *46* (4), 351−358.
(43) Dodd, P. M.; Jayaraman, A. Monte carlo simulations of polydisperse polymers grafted on spherical surfaces. *Journal of Polymer Science Part B: Polymer Physics* **2012**, *50* (10), 694−705.
(44) Nair, N.; Jayaraman, A. Self-Consistent PRISM Theory−Monte Carlo Simulation Studies of Copolymer Grafted Nanoparticles in a Homopolymer Matrix. *Macromolecules* **2010**, *43* (19), 8251−8263.


https://doi.org/10.1021/acs.macromol.4c00235
*Macromolecules* XXXX, XXX, XXX−XXX

(45) Costanzo, P. J.; Beyer, F. L. Thermally Driven Assembly of Nanoparticles in Polymer Matrices. *Macromolecules* **2007**, *40* (11), 3996−4001.
(46) Xu, C.; Ohno, K.; Ladmiral, V.; Composto, R. J. Dispersion of polymer-grafted magnetic nanoparticles in homopolymers and block copolymers. *Polymer* **2008**, *49* (16), 3568−3577.
(47) Goel, V.; Pietrasik, J.; Dong, H.; Sharma, J.; Matyjaszewski, K.; Krishnamoorti, R. Structure of Polymer Tethered Highly Grafted Nanoparticles. *Macromolecules* **2011**, *44* (20), 8129−8135.
(48) Green, P. F. The structure of chain end-grafted nanoparticle/homopolymer nanocomposites. *Soft Matter* **2011**, *7* (18), 7914−7926.
(49) Maillard, D.; Kumar, S. K.; Rungta, A.; Benicewicz, B. C.; Prudhomme, R. E. Polymer-Grafted-Nanoparticle Surfactants. *Nano Lett.* **2011**, *11* (11), 4569−4573.
(50) Jiao, Y.; Akcora, P. Assembly of Polymer-Grafted Magnetic Nanoparticles in Polymer Melts. *Macromolecules* **2012**, *45* (8), 3463−3470.
(51) Srivastava, S.; Agarwal, P.; Archer, L. A. Tethered Nanoparticle−Polymer Composites: Phase Stability and Curvature. *Langmuir* **2012**, *28* (15), 6276−6281.
(52) Ethier, J. G.; Hall, L. M. Structure and Entanglement Network of Model Polymer-Grafted Nanoparticle Monolayers. *Macromolecules* **2018**, *51* (23), 9878−9889.
(53) Ethier, J. G.; Drummy, L. F.; Vaia, R. A.; Hall, L. M. Uniaxial Deformation and Crazing in Glassy Polymer-Grafted Nanoparticle Ultrathin Films. *ACS Nano* **2019**, *13* (11), 12816−12829.
(54) Jayaraman, A. Polymer grafted nanoparticles: Effect of chemical and physical heterogeneity in polymer grafts on particle assembly and dispersion. *Journal of Polymer Science Part B: Polymer Physics* **2013**, *51* (7), 524−534.
(55) Abdilla, A.; Dolinski, N. D.; De Roos, P.; Ren, J. M.; Van Der Woude, E.; Seo, S. E.; Zayas, M. S.; Lawrence, J.; Read de Alaniz, J.; Hawker, C. J. Polymer stereocomplexation as a scalable platform for nanoparticle assembly. *J. Am. Chem. Soc.* **2020**, *142* (4), 1667−1672.
(56) Lawrence, J.; Pham, J. T.; Lee, D. Y.; Liu, Y.; Crosby, A. J.; Emrick, T. Highly Conductive Ribbons Prepared by Stick−Slip Assembly of Organosoluble Gold Nanoparticles. *ACS nano* **2014**, *8* (2), 1173−1179.
(57) Pham, J. T.; Lawrence, J.; Lee, D. Y.; Grason, G. M.; Emrick, T.; Crosby, A. J. Highly stretchable nanoparticle helices through geometric asymmetry and surface forces. *Adv. Mater.* **2013**, *25* (46), 6703−6708.
(58) Chen, X.; Lawrence, J.; Parelkar, S.; Emrick, T. Novel zwitterionic copolymers with dihydrolipoic acid: synthesis and preparation of nonfouling nanorods. *Macromolecules* **2013**, *46* (1), 119−127.
(59) Lee, D. Y.; Pham, J. T.; Lawrence, J.; Lee, C. H.; Parkos, C.; Emrick, T.; Crosby, A. J. Macroscopic nanoparticle ribbons and fabrics. *Advanced materials* **2013**, *25* (9), 1248−1253.
(60) Lawrence, J.; Emrick, T. Pentafluorophenyl ester-functionalized nanoparticles as a versatile platform for selective and covalent inter-nanoparticle coupling. *ACS Applied Materials & Interfaces* **2016**, *8* (3), 2393−2398.
(61) Priolo, M. A.; Gamboa, D.; Holder, K. M.; Grunlan, J. C. Super gas barrier of transparent polymer−clay multilayer ultrathin films. *Nano letters* **2010**, *10* (12), 4970−4974.
(62) Bay, R. K.; Zarybnicka, K.; Jančář, J.; Crosby, A. J. Mechanical Properties of Ultrathin Polymer Nanocomposites. *ACS Applied Polymer Materials* **2020**, *2* (6), 2220−2227.
(63) Crosby, A. J.; Lee, J. Y. Polymer nanocomposites: the "nano" effect on mechanical properties. *Polymer reviews* **2007**, *47* (2), 217−229.
(64) Bilchak, C. R.; Buenning, E.; Asai, M.; Zhang, K.; Durning, C. J.; Kumar, S. K.; Huang, Y.; Benicewicz, B. C.; Gidley, D. W.; Cheng, S.; et al. Polymer-Grafted Nanoparticle Membranes with Controllable Free Volume. *Macromolecules* **2017**, *50* (18), 7111−7120.
(65) Corbierre, M. K.; Cameron, N. S.; Sutton, M.; Laaziri, K.; Lennox, R. B. Gold nanoparticle/polymer nanocomposites: dispersion of nanoparticles as a function of capping agent molecular weight and grafting density. *langmuir* **2005**, *21* (13), 6063−6072.
(66) Borukhov, I.; Leibler, L. Enthalpic stabilization of brush-coated particles in a polymer melt. *Macromolecules* **2002**, *35* (13), 5171−5182.
(67) Kumar, S. K.; Jouault, N.; Benicewicz, B.; Neely, T. Nanocomposites with polymer grafted nanoparticles. *Macromolecules* **2013**, *46* (9), 3199−3214.
(68) Neha; Kant, R. Static Structure Factor and Viscoelastic Properties of Dendrimer Grafted Nanoparticles in Solution. *The Journal of Physical Chemistry B* **2021**, *125* (7), 1951−1959.
(69) Modica, K. J.; Martin, T. B.; Jayaraman, A. Effect of Polymer Architecture on the Structure and Interactions of Polymer Grafted Particles: Theory and Simulations. *Macromolecules* **2017**, *50* (12), 4854−4866.
(70) Ogbonna, N. D.; Dearman, M.; Bharti, B.; Peters, A. J.; Lawrence, J. Elucidating the impact of side chain dispersity on the assembly of bottlebrush polymers at the air-water interface. *J. Polym. Sci.* **2021**, *59*, 2458.
(71) Douglas, J. F.; Roovers, J.; Freed, K. F. Characterization of branching architecture through "universal" ratios of polymer solution properties. *Macromolecules* **1990**, *23* (18), 4168−4180.
(72) Likos, C. N.; Rosenfeldt, S.; Dingenouts, N.; Ballauff, M.; Lindner, P.; Werner, N.; Vögtle, F. Gaussian effective interaction between flexible dendrimers of fourth generation: A theoretical and experimental study. *The Journal of Chemical Physics* **2002**, *117* (4), 1869−1877.
(73) Sun, W. Functionalization of surfaces with branched polymers. *RSC Advances* **2016**, *6* (48), 42089−42108.
(74) Lebedeva, I. O.; Zhulina, E. B.; Leermakers, F. A. M.; Borisov, O. V. Dendron and Hyperbranched Polymer Brushes in Good and Poor Solvents. *Langmuir* **2017**, *33* (5), 1315−1325.
(75) LaNasa, J. A.; Hickey, R. J. Surface-Initiated Ring-Opening Metathesis Polymerization: A Method for Synthesizing Polymer-Functionalized Nanoparticles Exhibiting Semicrystalline Properties and Diverse Macromolecular Architectures. *Macromolecules* **2020**, *53* (19), 8216−8232.
(76) Doyen, M.; Goole, J.; Bartik, K.; Bruylants, G. Amino acid induced fractal aggregation of gold nanoparticles: Why and how. *J. Colloid Interface Sci.* **2016**, *464*, 160−166.
(77) Häkkinen, H. The gold−sulfur interface at the nanoscale. *Nature Chemistry* **2012**, *4* (6), 443−455.
(78) Badia, A.; Demers, L.; Dickinson, L.; Morin, F. G.; Lennox, R. B.; Reven, L. Gold−Sulfur Interactions in Alkylthiol Self-Assembled Monolayers Formed on Gold Nanoparticles Studied by Solid-State NMR. *J. Am. Chem. Soc.* **1997**, *119* (45), 11104−11105.
(79) Lin, S.-Y.; Tsai, Y.-T.; Chen, C.-C.; Lin, C.-M.; Chen, C.-H. Two-Step Functionalization of Neutral and Positively Charged Thiols onto Citrate-Stabilized Au Nanoparticles. *The Journal of Physical Chemistry B* **2004**, *108* (7), 2134−2139.
(80) Retout, M.; Brunetti, E.; Valkenier, H.; Bruylants, G. Limits of thiol chemistry revealed by quantitative analysis of mixed layers of thiolated-PEG ligands grafted onto gold nanoparticles. *J. Colloid Interface Sci.* **2019**, *557*, 807−815.
(81) Martin, T. B.; Dodd, P. M.; Jayaraman, A. Polydispersity for Tuning the Potential of Mean Force between Polymer Grafted Nanoparticles in a Polymer Matrix. *Phys. Rev. Lett.* **2013**, *110* (1), No. 018301.
(82) Smith, J. S.; Bedrov, D.; Smith, G. D. A molecular dynamics simulation study of nanoparticle interactions in a model polymer-nanoparticle composite. *Compos. Sci. Technol.* **2003**, *63* (11), 1599−1605.
(83) Nikoubashman, A.; Lee, V. E.; Sosa, C.; Prudhomme, R. K.; Priestley, R. D.; Panagiotopoulos, A. Z Directed Assembly of Soft Colloids through Rapid Solvent Exchange. *ACS Nano* **2016**, *10* (1), 1425−1433.
(84) Kremer, K.; Grest, G. S. Dynamics of entangled linear polymer melts: A molecular-dynamics simulation. *The Journal of Chemical Physics* **1990**, *92* (8), 5057−5086.


https://doi.org/10.1021/acs.macromol.4c00235
*Macromolecules* XXXX, XXX, XXX−XXX

(85) Li, N.; Nikoubashman, A.; Panagiotopoulos, A. Z. Self-Assembly of Polymer Blends and Nanoparticles through Rapid Solvent Exchange. *Langmuir* **2019**, *35* (10), 3780−3789.
(86) Everaers, R.; Ejtehadi, M. R. Interaction potentials for soft and hard ellipsoids. *Phys. Rev. E* **2003**, *67* (4), No. 041710, DOI: 10.1103/physreve.67.041710.
(87) Visser, J. On Hamaker constants: A comparison between Hamaker constants and Lifshitz-van der Waals constants. *Adv. Colloid Interface Sci.* **1972**, *3* (4), 331−363.
(88) Anderson, J. A.; Glaser, J.; Glotzer, S. C. HOOMD-blue: A Python package for high-performance molecular dynamics and hard particle Monte Carlo simulations. *Comput. Mater. Sci.* **2020**, *173*, No. 109363.
(89) Ovy, S. M. A. I.; Obinwa, J.; Peters, A. J. The Effect of Graft Density on the Ordering of Block Copolymer Grafted Nanoparticles. *Macromolecules* **2020**, *53* (23), 10655−10663.
(90) Roux, B. The calculation of the potential of mean force using computer simulations. *Comput. Phys. Commun.* **1995**, *91* (1), 275−282.
(91) Kumar, S.; Rosenberg, J. M.; Bouzida, D.; Swendsen, R. H.; Kollman, P. A. THE weighted histogram analysis method for free-energy calculations on biomolecules. I. The method. *J. Comput. Chem.* **1992**, *13* (8), 1011−1021.
(92) Grossfield, A. *WHAM: the weighted histogram analysis method*. 2003. http://membrane.urmc.rochester.edu/wordpress/?page_id=126.
(93) Martín-Sánchez, C.; Sánchez-Iglesias, A.; Barreda-Argüeso, J. A.; Polian, A.; Liz-Marzán, L. M.; Rodríguez, F. Behavior of Au Nanoparticles under Pressure Observed by In Situ Small-Angle X-ray Scattering. *ACS Nano* **2023**, *17* (1), 743−751.
(94) Matsen, M. W.; Gardiner, J. Autophobic dewetting of homopolymer on a brush and entropic attraction between opposing brushes in a homopolymer matrix. *The Journal of Chemical Physics* **2001**, *115* (6), 2794−2804.
(95) Arkın, H.; Janke, W. Gyration tensor based analysis of the shapes of polymer chains in an attractive spherical cage. *J. Chem. Phys.* **2013**, *138* (5), No. 054904.
(96) Yun, H.; Yu, J. W.; Lee, Y. J.; Kim, J.-S.; Park, C. H.; Nam, C.; Han, J.; Heo, T.-Y.; Choi, S.-H.; Lee, D. C.; et al. Symmetry Transitions of Polymer-Grafted Nanoparticles: Grafting Density Effect. *Chem. Mater.* **2019**, *31* (14), 5264−5273.
(97) Kim, B. J.; Bang, J.; Hawker, C. J.; Kramer, E. J. Effect of Areal Chain Density on the Location of Polymer-Modified Gold Nanoparticles in a Block Copolymer Template. *Macromolecules* **2006**, *39* (12), 4108−4114.


https://doi.org/10.1021/acs.macromol.4c00235
*Macromolecules* XXXX, XXX, XXX−XXX